



RESEARCH ARTICLE | FEBRUARY 24 2022

Oxygen vacancy dynamics in monoclinic metallic VO₂ domain structures

Dustin Schrecongost; Hai-Tian Zhang; Roman Engel-Herbert; Cheng Cen  

 Check for updates

Appl. Phys. Lett. 120, 081602 (2022)

<https://doi.org/10.1063/5.0083771>

 CHORUS



View Online



Export Citation

CrossMark

Articles You May Be Interested In

Shear strain stabilized high-temperature metallic monoclinic VO₂ variants with symmetry permission

Appl. Phys. Lett. (March 2023)

Study of interaction of nucleobases with ultrathin VO₂ monoclinic nanowire

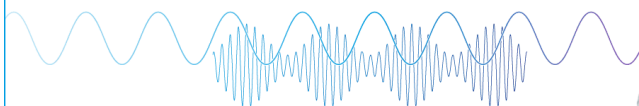
AIP Conference Proceedings (August 2019)

Formation energies of intrinsic point defects in monoclinic VO₂ studied by first-principles calculations

AIP Advances (October 2016)

Webinar

Boost Your Signal-to-Noise Ratio with Lock-in Detection



Sep. 7th – Register now



Zurich Instruments

Oxygen vacancy dynamics in monoclinic metallic VO₂ domain structures

Cite as: Appl. Phys. Lett. **120**, 081602 (2022); doi: [10.1063/5.0083771](https://doi.org/10.1063/5.0083771)

Submitted: 29 December 2021 · Accepted: 14 February 2022 ·

Published Online: 24 February 2022



View Online



Export Citation



CrossMark

Dustin Schrecongost,^{1,2} Hai-Tian Zhang,³ Roman Engel-Herbert,³ and Cheng Cen^{1,a)} 

AFFILIATIONS

¹Department of Physics and Astronomy, West Virginia University, Morgantown, West Virginia 26506, USA

²RJ Lee Group, Monroeville, Pennsylvania 15146, USA

³Department of Materials Science and Engineering, Pennsylvania State University, University Park, Pennsylvania 16802, USA

^{a)}Author to whom correspondence should be addressed: cheng.cen@mail.wvu.edu

ABSTRACT

It was demonstrated recently that the nano-optical and nanoelectronic properties of VO₂ can be spatially programmed through the local injection of oxygen vacancies by atomic force microscope writing. In this work, we study the dynamic evolution of the patterned domain structures as a function of the oxygen vacancy concentration and the time. A threshold doping level is identified that is critical for both the metal–insulator transition and the defect stabilization. The diffusion of oxygen vacancies in the monoclinic phase is also characterized, which is directly responsible for the short lifetimes of sub-100 nm domain structures. This information is imperative for the development of oxide nanoelectronics through defect manipulations.

Published under an exclusive license by AIP Publishing. <https://doi.org/10.1063/5.0083771>

The control and manipulation of oxygen vacancies (OVs)¹ have enabled a great variety of designed functionalities in metal oxides, such as magnetism,² superconductivity,³ and two dimensional electron gas.^{4,5} In vanadium dioxide (VO₂),^{6,7} the creation of OVs can effectively suppress the metal–insulator transition (MIT) near room temperature.⁸ Our recent works demonstrated the nanoscale control of the MIT in VO₂ by conducting atomic force microscope (AFM) writing.^{9,10} A biased AFM probe is used to locally inject OVs into the monoclinic insulating (MI-phase) film and creates metallic domains without changing the monoclinic lattice symmetry (MM-phase). In MM-phase domains written by AFM, the accumulation of OVs produces a 3% lattice expansion along the monoclinic *a*-axis¹⁰ and also significant electron doping. The resultant drastically changed optical and electrical characteristics, which allow a series of on-demand nanoplasmonic devices to be fabricated,⁹ all based on designed OV distributions in this monolithic material platform.

The development of OV-based device applications requires a deep understanding of the charge transfer induced by the OV formation as well as the dynamics of their annihilation and migration. Here, we study these mechanisms in monoclinic VO₂ utilizing AFM-tailored domain structures with varied sizes and OV concentrations. The transient evolution of these domains is monitored using a multi-channel scanning probe microscopy technique that images the near-field optical signal and the surface electrical properties simultaneously. The

measurement results directly quantify the doping threshold needed for triggering MIT through OV injection and the rate of in-plane OV diffusion, providing valuable information needed for improving the stability and density of the MM-phase domain structures in the future.

30 nm thick VO₂ films used in this study are grown on *r*-plane Al₂O₃ by molecular beam epitaxy (MBE)¹¹ with the monoclinic *a*-axis oriented out-of-plane. To elucidate the correlation between the writing induced change in the doping and the resultant electronic phase transition, we use a unique multi-channel scanning probe imaging technique¹² [Fig. 1(a)], which is capable of acquiring scattering-type scanning near-field optical microscope (s-SNOM) signal and Kelvin probe force microscopy (KPFM) signal simultaneously. In this setup, a platinum coated AFM probe is both mechanically driven by a piezo at the resonance frequency of the cantilever (Ω) and electrically modulated at a much lower frequency (ω). The s-SNOM signal is detected by demodulating the probe scattered light at harmonics of Ω , and the KPFM surface potential is readout as the nulling bias that minimizes the probe dither at the sideband frequency $\Omega + \omega$. The detailed methodology is described in Ref. 12.

Using this setup, the local doping level is quantified by the KPFM surface potential data, and the electronic phase transition is identified by the mid-infrared ($\lambda = 10.9 \mu\text{m}$) s-SNOM signal.^{7,9,10,13} Figures 1(b) and 1(c) show the KPFM and s-SNOM images taken on a 4×3 dot matrix written by AFM. Each dot is created by a single voltage pulse

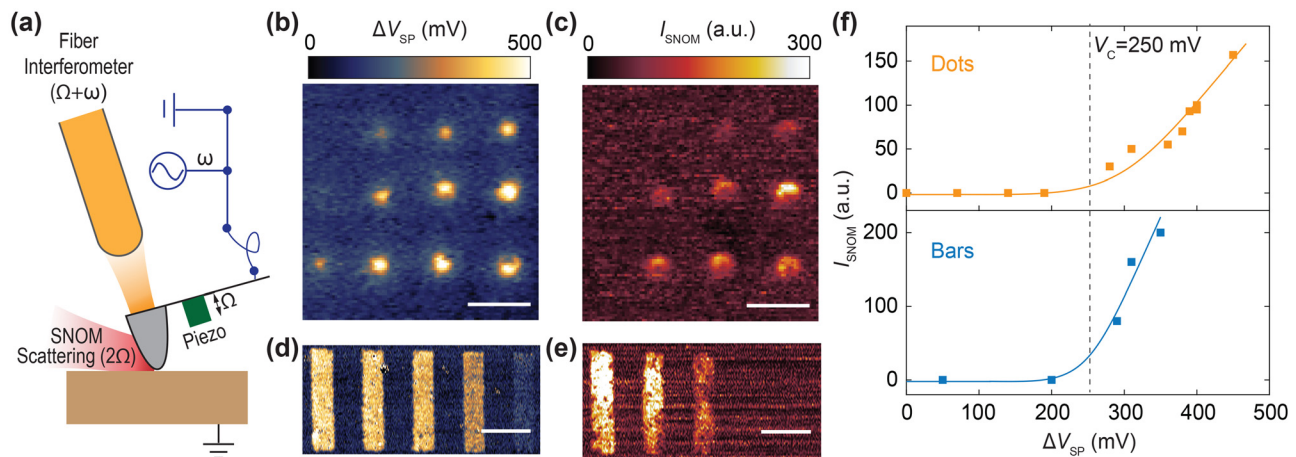


FIG. 1. Doping threshold of the transition to the monoclinic metallic phase. (a) Schematic setup of the multi-channel scanning probe imaging method. KPFM (b) and s-SNOM (c) images acquired simultaneously on an array of dots written with different dosages. From top to bottom, the writing biases used in each row are 30, 40, and 50 V. From left to right, the writing bias durations used in each column are 100, 150, 200, and 250 ms. (d) and (e) Similar images as in (b) and (c) but acquired on an array of bar structures. From left to right, the writing bias reduces from 10 to 2 V in an increment of -2 V, and the writing scan speed is kept at $1 \mu\text{m/s}$. All scale bars in (b)–(e) represent $1 \mu\text{m}$. (f) Correlation between the s-SNOM and KPFM contrasts showing a minimum surface potential increase in 250 mV needed for the transition into the MM phase.

applied to a stationary AFM probe in contact with the sample surface. From top to bottom, the pulse amplitude increases from 30 to 50 V in 10 V increments. From left to right, the pulse duration increases from 100 to 250 ms with 50 ms increments. In addition, an array of bars with larger domain areas is also studied, which are written by raster scans at a 50 nm line space [Figs. 1(d) and 1(e)]. In this case, from left to right, the probe bias varies from 10 to 2 V with a step of -2 V, and a constant scan speed is used during writing ($1 \mu\text{m/s}$). We note that KPFM and s-SNOM imaging of these written structures are all performed at least 20 min after the writing. Such delay is to allow the writing induced surface charges to dissipate and the perturbed surface adsorption to re-equilibrate, such that the measurement data can be reliably compared to reveal the intrinsic material changes.

For both structure types, the surface potential of the written region increases as the writing dosage becomes larger, which is consistent with the expected trend that a larger density of probe-injected OV's will produce a more significant electron doping, thus a smaller work function. It should be noted that probe-induced surface potential changes in oxides may result from several different mechanisms,^{5,14} such as ion redistribution, modification of the surface adsorbates, and the formation of local polarizations. However, as shown by the structural and compositional measurements discussed in our previous work,¹⁰ the effect of the positively biased probe writing in our VO_2 film is dominated by surface water assisted creation of OV's. Interestingly, the writing dosage per unit area required for the isolated nanodots is much larger compared to what is needed for writing the much larger bars. Also, comparing the KPFM and s-SNOM images, one finds that the signals from the two channels do not correlate with each other linearly. Some structures that are clearly resolved by KPFM, such as the first dot in the third row or the fourth bar, are completely invisible from the s-SNOM images. Figure 1(f) plots the s-SNOM contrast of each written structure vs their KPFM surface potential [$\Delta V_{SP} = V_{SP}(\text{written region}) - V_{SP}(\text{unwritten region})$]. In both cases, the generation of a nonzero s-SNOM contrast requires

ΔV_{SP} to exceed a threshold value of $V_C = 250$ mV, which means that the AFM writing needs to raise the Fermi level (ΔE_F^{MIT}) by at least 250 meV in order to produce a metal-insulator transition. As shown by our earlier report,¹⁰ the temperature-dependent resistivity of the unwritten MI-phase region exhibits an Arrhenius-type insulating behavior with an activation energy of $E_A^{MI} = E_C - E_F \approx 130$ meV. In a regular semiconductor, a raise of the Fermi level by 130 meV will be adequate to produce a metallic phase, which is, however, much less the 250 meV threshold value observed here. Such discrepancy indicates that the introduction of OV's by AFM writing, while leaving the monoclinic lattice structure intact, most likely significantly modifies the electronic band structure.¹⁵

Another threshold behavior associated with the same critical doping level is observed when monitoring the transient evolution of the AFM written structures. Figures 2(a) and 2(b) show the s-SNOM and KPFM images of a $4 \times 4 \mu\text{m}^2$ square taken on different days after the initial AFM writing. Due to the depletion of OV's via the oxygen exchange with the atmosphere^{10,16} [Fig. 2(f)], the MM-phase produced by AFM writing reverts back to the MI-phase in around nine days. Such depletion can be suppressed by storing the written structure in a high vacuum chamber with a pressure below 10^{-5} mbar [Figs. 2(e) and 2(f)]. Analyzing the daily measurement results shown in Figs. 2(a) and 2(b) more carefully, we find that the transient changes are very gradual during the first five days but expedites significantly afterward. Plotting the averaged ΔV_{SP} inside the square region vs the time [Fig. 2(c)], we see that the turning point occurs when ΔV_{SP} falls below V_C . That is to say, the OV's in a MM-phase region are more stable than the ones in a MI-phase region. Such effect suggests that when the OV concentration in monoclinic VO_2 increases above the threshold value, not only do they trigger a metal-insulator transition, but also the strong electron-lattice correlation produces a profound change in the energy profile of the ionic defects.

While the air-assisted OV depletion process is the primary cause of the limited lifetime of the micrometer-scale structures, the evolution

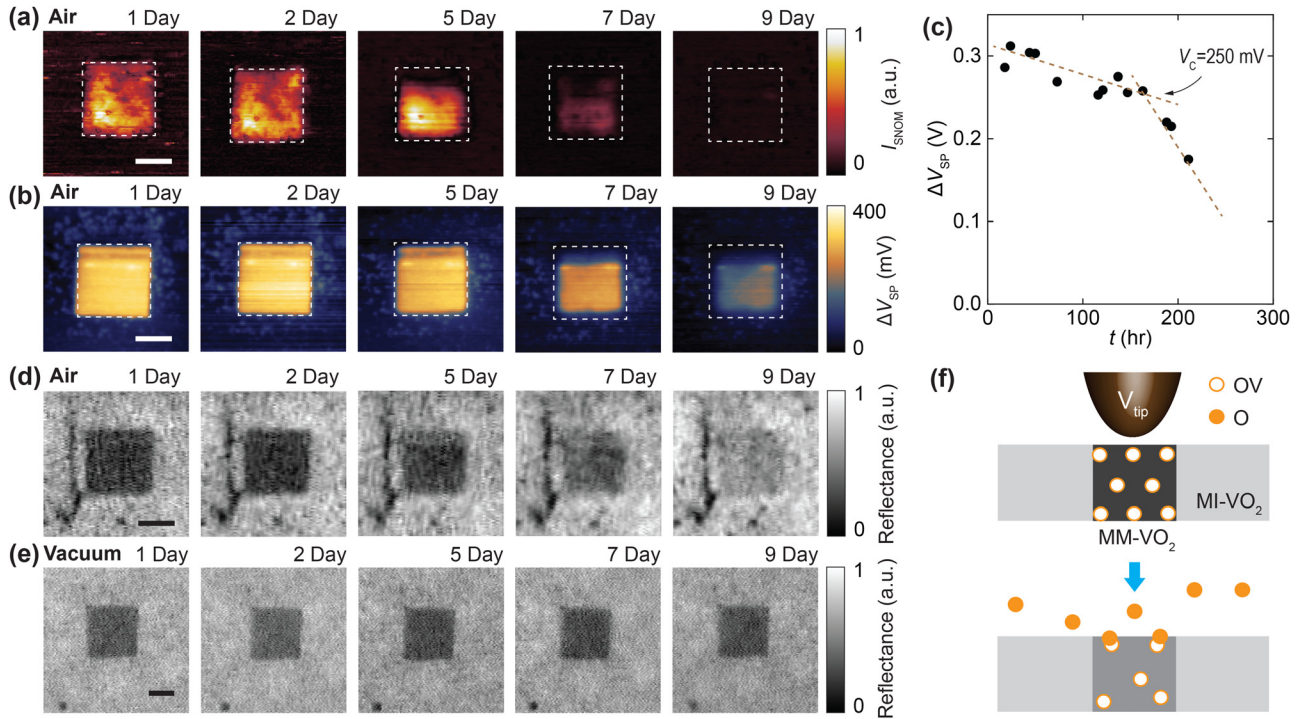


FIG. 2. Threshold behavior associated with the depletion of the oxygen vacancies in air (a) s-SNOM and (b) KPFM images of a $4 \times 4 \mu\text{m}^2$ square measured on different days after the initial AFM writing. (c) Transient change in the averaged surface potential inside the square region. (d) Sequential white-light optical microscopy images of a second square written in the same way. In air, (e) similar plots as (d) but for a square stored in a 10^{-5} mbar level vacuum after its creation. Scale bars in (a), (b), (d), and (e) all represent $2 \mu\text{m}$. (f) The time-dependent changes shown in (a)–(d) are attributed to the depletion of the OVs through the oxygen exchange with the atmosphere.

of the nanoscale structures is dominated by another mechanism. At room temperature, the thermally activated hopping of OVs can lead to their diffusion¹⁷ [Fig. 3(d)]. Figure 3(a) shows the KPFM measurements performed on two nanowire configurations: two isolated nanowires oriented perpendicular to each other and an array of closely spaced nanowires. Comparing the images taken immediately after the AFM writing and after 24 h, the surface potential profiles of the two isolated nanowires are clearly broadened [Fig. 3(b)], and the nanowires in the array become less distinguished from each other. V_{SP} decreases along each wire and increases in the gap between them [Fig. 3(e)]. These features are all hallmark characteristics of the diffusion process.

Assuming that the mobile carrier density is proportional to the dopant (i.e., OVs) concentration, we can more quantitatively link V_{SP} to the OV concentration in the following way. In a semiconductor, the density of mobile electrons can be expressed as $n = \int_{E_C}^{\infty} f(E)D(E)dE$, where E_C is the bottom of the conduction band, $f(E)$ is the Fermi-Dirac distribution function, and $D(E)$ is the density of states. For the measurement shown in Fig. 3, the writing dosage is kept low to make sure that all nanowires are still in the MI-phase, allowing the OV diffusion to be studied faithfully in a single material phase without the complications from phase boundaries or phase transitions. In such insulating state, where the Fermi level lies deep inside the bandgap ($E_C - E_F \gg kT$), the integral of the electron density can be approximated by $n \approx N^* e^{(E_F - E_C)/kT}$, where $N^* = 2(m^* kT/2\pi\hbar^2)^{3/2}$ is the effective density of states in the conduction band. Using the transport activation energy of the unwritten MI-phase region

($E_A^{MI} = E_C - E_F \approx 130$ meV) as a reference, the normalized carrier density in the written region can be estimated from the KPFM measurement following the relation:

$$n/N^* = \exp\left(\frac{-E_A^{MI} + \Delta V_{SP}}{kT}\right), \quad (1)$$

which traces the OV concentration in proportion.

The diffusion of OVs near nanowires can be modeled by the 1D equation $\frac{\partial n}{\partial t} = D \frac{\partial^2 n}{\partial x^2}$, where D is the in-plane diffusion constant. Starting from an initial Gaussian form of $n(t=0) = n_0 \exp(-x^2/w_0^2)$, the solution to the diffusion equation is

$$n(t) = \frac{w_0 n_0}{\sqrt{4Dt + w_0^2}} \exp\left(-\frac{x^2}{4Dt + w_0^2}\right). \quad (2)$$

From Eq. (2), it is clear that the in-plane OV diffusion will eventually wipe out the local accumulation of OVs, though the speed of this process is highly dependent on the diffusion constant D and the initial structure size w_0 . Fitting the full width at half maximum (FWHM) of the two isolated nanowires according to Eq. (2), a consistent diffusion constant of $D = 5 \times 10^{-20}$ m²/s is found in both cases [Fig. 3(c)]. This value, characterizing the rate of the OV diffusion in the plane perpendicular to the monoclinic a -axis, is three times smaller than the diffusion constant found in amorphous VO₂ films.¹⁸ The difference suggests that OV migration is faster along the monoclinic a -axis, consistent with the theory prediction.^{18,19} Comparing to other ionic dopants commonly

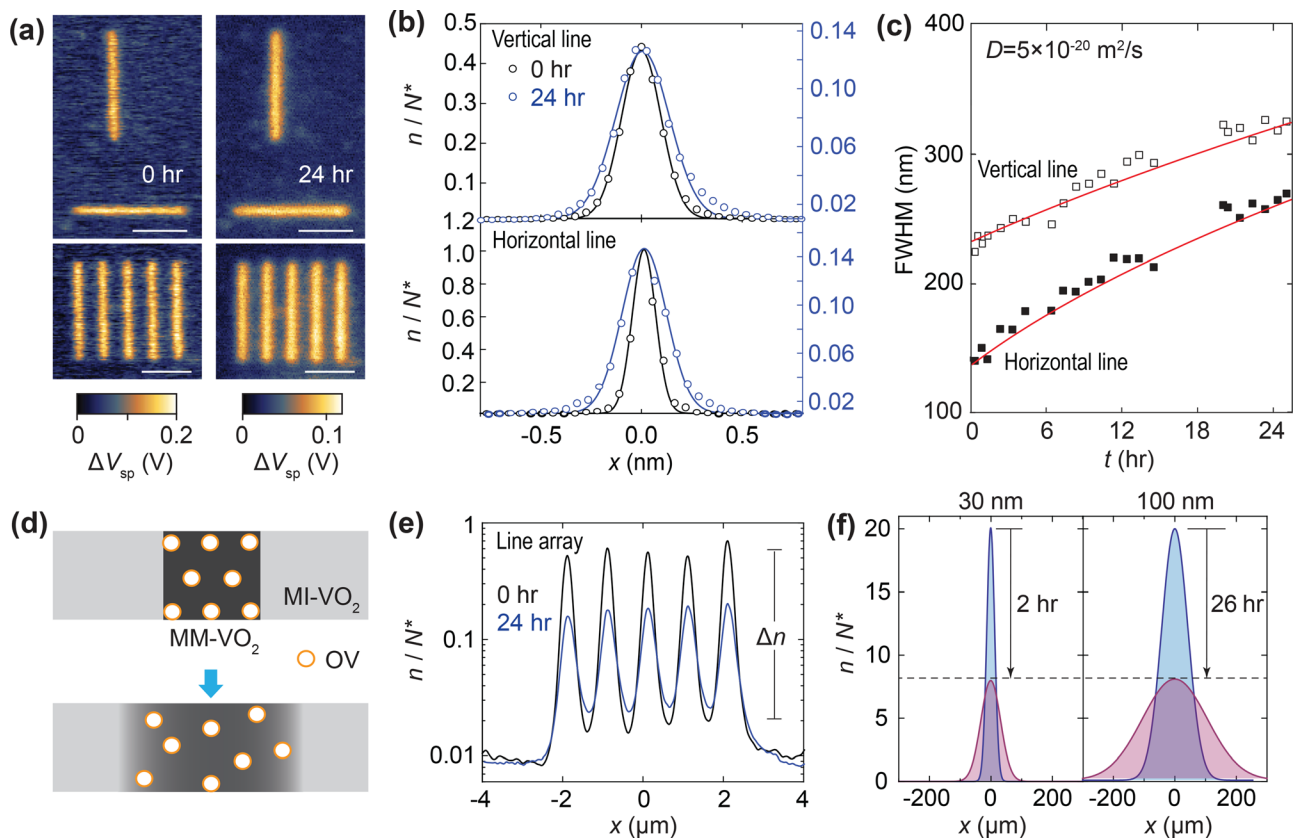


FIG. 3. In-plane diffusion of the oxygen vacancies. (a) KPFM images of two nanowire configurations taken immediately and 24 h after the AFM writing. The scale bars represent $2 \mu\text{m}$. (b) and (e) Carrier density profiles across the single nanowires (b) and the nanowire array (e). In (b), the hollow dots show the raw measurement data, and the solid curves are Gaussian fittings. (d) Illustration of the in-plane OV diffusion. (c) Time-dependent changes of the FWHMs of the two nanowires fitted by the 1D diffusion model following Eq. (2). (f) Calculated diffusion-induced carrier density profile evolutions of two nanowires with different widths.

used in VO_2 , such as hydrogen,²⁰ the diffusion constant of OVs is orders of magnitude smaller, likely due to the limited migration pathways and the higher activation barriers resulting from their larger size. Such feature makes OVs more suitable for nanoscale phase control.

The sensitive dependence of the diffusion process on w_0 explains why the writing dosage needed for patterning MM-phase nanostructures is so much larger than what is needed for larger domains (Fig. 1) and why it is so difficult to make MM-phase structures smaller than 100 nm by AFM writing.⁹ With a diffusion constant of $D = 5 \times 10^{-20} \text{ m}^2/\text{s}$, while it takes 26 h for the OV concentration in a 100 nm wide nanowire to drop by 60%, the duration of the same process reduces to only 2 h in a 30 nm wire [Fig. 3(f)]. The actual decay may be even faster because the OV diffusion will be significantly expedited by the probe field applied during the writing process, thus leaving almost no time for the sub-100 nm structures to be properly imaged in experiment. In comparison, when it comes to micrometer-scale structures such as the ones shown in Fig. 2, the very large w_0 makes the effect of the in-plane diffusion almost negligible.

In conclusion, we have studied the doping mechanism and the dynamic evolution of the AFM-written domains with tunable OV accumulations in VO_2 thin films. The collection of data shows that the metal-insulator transition induced by OVs does not occur as a pure

electrostatic process as in regular semiconductors, but rather involves a significant modification of the electronic band structure. We are also able to quantify the diffusion constant of the OVs in the plane perpendicular to the monoclinic a -axis. While already much smaller than other common ionic dopants, the $10^{-20} \text{ m}^2/\text{s}$ level D value found here still significantly impedes the patterning of sub-100 nm MM-phase domains. On the one hand, to better study the domain dynamics at such a small length scale, one solution is to perform AFM writing at cryogenic temperatures where, due to the greatly suppressed thermally activated OV hopping process, the nanostructures can maintain their designed dimensions for a much longer period. In addition, techniques for better confining the writing field, such as using shielded probes²¹ or filament based phase change probes,²² can also be explored to further minimize the field-driven OV migrations. On the other hand, to allow the fabrication of smaller nanoelectronic or nanophotonic devices that can stably operate at room temperature, it will be highly desirable to explore methods, such as strain engineering,²³ that can increase the energy barriers associated with the migration of OVs in VO_2 .

The experimental work at West Virginia University was supported by the Department of Energy under Grant No. DE-SC0021393. The work at Pennsylvania State University was supported

by the National Science Foundation through Grant No. DMR-1352502 and the Penn State Materials Research Science and Engineering Centers Program No. DMR-1420620.

AUTHOR DECLARATIONS

Conflict of Interest

The authors declare no conflict of interest.

DATA AVAILABILITY

The data that support the findings of this study are available from the corresponding author upon reasonable request.

REFERENCES

- ¹F. Gunkel, D. V. Christensen, Y. Z. Chen, and N. Pryds, *Appl. Phys. Lett.* **116**(12), 120505 (2020).
- ²M. Salluzzo, S. Gariglio, D. Stornaiuolo, V. Sessi, S. Rusponi, C. Piamonteze, G. M. De Luca, M. Minola, D. Marré, A. Gadaleta, H. Brune, F. Nolting, N. B. Brookes, and G. Ghiringhelli, *Phys. Rev. Lett.* **111**(8), 087204 (2013).
- ³C. W. Rischau, X. Lin, C. P. Grams, D. Finck, S. Harms, J. Engelmayer, T. Lorenz, and Y. Gallais, *Nat. Phys.* **13**(7), 643 (2017).
- ⁴H. Zhang, Y. Yun, X. Zhang, H. Zhang, Y. Ma, X. Yan, F. Wang, G. Li, R. Li, T. Khan, Y. Chen, W. Liu, F. Hu, B. Liu, B. Shen, W. Han, and J. Sun, *Phys. Rev. Lett.* **121**(11), 116803 (2018).
- ⁵W. Dai, M. Yang, H. Lee, J.-W. Lee, C.-B. Eom, and C. Cen, *Nano Lett.* **17**(9), 5620 (2017).
- ⁶T. M. Rice, H. Launois, and J. P. Pouget, *Phys. Rev. Lett.* **73**(22), 3042 (1994); S. Biermann, A. Poteryaev, A. I. Lichtenstein, and A. Georges, *ibid.* **94**(2), 026404 (2005); M. W. Haverkort, Z. Hu, A. Tanaka, W. Reichelt, S. V. Streltsov, M. A. Korotin, V. I. Anisimov, H. H. Hsieh, H. J. Lin, C. T. Chen, D. I. Khomskii, and L. H. Tjeng, *ibid.* **95**(19), 196404 (2005); M. Currie, M. A. Mastro, and V. D. Wheeler, *Opt. Mater. Express* **7**(5), 1697 (2017); M. A. Kats, R. Blanchard, P. Genevet, Z. Yang, M. M. Qazilbash, D. N. Basov, S. Ramanathan, and F. Capasso, *Opt. Lett.* **38**(3), 368 (2013); M. J. Dicken, K. Aydin, I. M. Pryce, L. A. Sweatlock, E. M. Boyd, S. Walavalkar, J. Ma, and H. A. Atwater, *Opt. Express* **17**(20), 18330 (2009); S.-J. Kim, H. Yun, K. Park, J. Hong, J.-G. Yun, K. Lee, J. Kim, S. J. Jeong, S.-E. Mun, and J. Sung, *Sci. Rep.* **7**, 43723 (2017); Z. Zhu, Z. Coppens, P. Evans, R. Haglund, J. Valentine, J.-Y. Ou, E. Plum, L. Jiang, and N. I. Zheludev, *Nano Lett.* **11**(5), 2142 (2011).
- ⁷M. M. Qazilbash, M. Brehm, B.-G. Chae, P.-C. Ho, G. O. Andreev, B.-J. Kim, S. J. Yun, A. V. Balatsky, M. B. Maple, F. Keilmann, H.-T. Kim, and D. N. Basov, *Science* **318**(5857), 1750 (2007).
- ⁸J. Jeong, N. Aetukuri, T. Graf, T. D. Schladt, M. G. Samant, and S. S. P. Parkin, *Science* **339**(6126), 1402 (2013).
- ⁹D. Schrecongost, Y. Xiang, J. Chen, C. Ying, H.-T. Zhang, M. Yang, P. Gajurel, W. Dai, R. Engel-Herbert, and C. Cen, *Nano Lett.* **20**(10), 7760 (2020).
- ¹⁰D. Schrecongost, M. Aziziha, H. Zhang, I. Tung, J. Tessmer, W. Dai, Q. Wang, R. Engel-Herbert, H. Wen, and Y. N. Picard, *Adv. Funct. Mater.* **29**, 1905585 (2019).
- ¹¹H.-T. Zhang, L. Zhang, D. Mukherjee, Y.-X. Zheng, R. C. Haislmaier, N. Alem, and R. Engel-Herbert, *Nat. Commun.* **6**, 8475 (2015).
- ¹²D. Schrecongost, *On Demand Nanoscale Phase Manipulation of Vanadium Dioxide by Scanning Probe Lithography* (West Virginia University, 2020).
- ¹³A. C. Jones, S. Berweger, J. Wei, D. Cobden, and M. B. Raschke, *Nano Lett.* **10**(5), 1574 (2010).
- ¹⁴S. Adhikari, A. C. Garcia-Castro, A. H. Romero, H. Lee, J.-W. Lee, S. Ryu, C.-B. Eom, and C. Cen, *Adv. Funct. Mater.* **26**(30), 5453 (2016); W. Dai, S. Adhikari, A. C. Garcia-Castro, A. H. Romero, H. Lee, J.-W. Lee, S. Ryu, C.-B. Eom, and C. Cen, *Nano Lett.* **16**(4), 2739 (2016); F. Bi, D. F. Bogorin, C. Cen, C. W. Bark, J.-W. Park, C.-B. Eom, and J. Levy, *Appl. Phys. Lett.* **97**(17), 173110 (2010); M. Andrá, F. Gunkel, C. Bäumer, C. Xu, R. Dittmann, and R. Waser, *Nanoscale* **7**(34), 14351 (2015); S. Das, B. Wang, Y. Cao, M. R. Cho, Y. J. Shin, S. M. Yang, L. Wang, M. Kim, S. V. Kalinin, L.-Q. Chen, and T. W. Noh, *Nat. Commun.* **8**(1), 615 (2017); E. Ferreiro-Vila, S. Blanco-Canosa, I. L. del Pozo, H. B. Vasili, C. Magén, A. Ibarra, J. Rubio-Zuazo, G. R. Castro, L. Morellón, and F. Rivadulla, *Adv. Funct. Mater.* **29**(48), 1901984 (2019); Y. Sharma, J. Balachandran, C. Sohn, J. T. Krogel, P. Ganesh, L. Collins, A. V. Ievlev, Q. Li, X. Gao, N. Balke, O. S. Ovchinnikova, S. V. Kalinin, O. Heinonen, and H. N. Lee, *ACS Nano* **12**(7), 7159 (2018).
- ¹⁵Z. Li, J. Wu, Z. Hu, Y. Lin, Q. Chen, Y. Guo, Y. Liu, Y. Zhao, J. Peng, W. Chu, C. Wu, and Y. Xie, *Nat. Commun.* **8**(1), 15561 (2017); Z. Shao, X. Cao, H. Luo, and P. Jin, *NPG Asia Mater.* **10**(7), 581 (2018); L. Fan, X. Wang, F. Wang, Q. Zhang, L. Zhu, Q. Meng, B. Wang, Z. Zhang, and C. Zou, *RSC Adv.* **8**(34), 19151 (2018).
- ¹⁶P. Gorai, Y. V. Kondratenko, and E. G. Seebauer, *J. Appl. Phys.* **111**(9), 094510 (2012); R. Schaub, E. Wahlström, A. Ronnau, E. Lægsgaard, I. Stensgaard, and F. Besenbacher, *Science* **299**(5605), 377 (2003); S. Bao, J. Ma, T. Yang, M. Chen, J. Chen, S. Pang, C.-W. Nan, and C. Chen, *ACS Appl. Mater. Interfaces* **10**(5), 5107 (2018).
- ¹⁷R. A. De Souza, *Adv. Funct. Mater.* **25**(40), 6326 (2015).
- ¹⁸P. P. Boriskov, M. A. Belyaev, and A. A. Velichko, *Russ. J. Phys. Chem.* **91**(6), 1064 (2017).
- ¹⁹D. Passarello, S. G. Altendorf, J. Jeong, C. Rettner, N. Arellano, T. Topuria, M. G. Samant, and S. S. P. Parkin, *Nano Lett.* **17**(5), 2796 (2017); J. Jeong, N. B. Aetukuri, D. Passarello, S. D. Conradson, M. G. Samant, and S. S. P. Parkin, *Proc. Natl. Acad. Sci. U. S. A.* **112**(4), 1013 (2015).
- ²⁰K. Muraoka and T. Kanki, *Sci. Rep.* **9**(1), 20093 (2019); J. Lin, H. Ji, M. W. Swift, W. J. Hardy, Z. Peng, X. Fan, A. H. Nevidomskyy, J. M. Tour, and D. Natelson, *Nano Lett.* **14**(9), 5445 (2014).
- ²¹K. A. Brown, K. J. Satzinger, and R. M. Westervelt, *Nanotechnol.* **23**(11), 115703 (2012).
- ²²E. Soh, G. Syed, G. Mazzotta, B. F. Porter, M. K. Riede, R. Nicholas, J. S. Kim, and H. Bhaskaran, *Nano Lett.* **20**, 1067 (2020).
- ²³U. Aschauer, R. Pfenninger, S. M. Selbach, T. Grande, and N. A. Spaldin, *Phys. Rev. B* **88**(5), 054111 (2013).